AGU PUBLICATIONS

JGR

Journal of Geophysical Research: Space Physics

TECHNICAL REPORTS: METHODS

10.1002/2016JA022700

Special Section:
Measurement Techniques in Solar and Space Physics: Photons

Calibration and testing of wide-field UV instruments

H. U. Frey[1], S. B. Mende[1], J. Loicq[2], and S. Habraken[2]

[1]Space Sciences Laboratory, University of California, Berkeley, California, USA, [2]Centre Spatial de Liège, Liège, Belgium

Abstract As with all optical systems the calibration of wide-field ultraviolet (UV) systems includes three main areas: sensitivity, imaging quality, and imaging capability. The one thing that makes UV calibrations difficult is the need for working in vacuum substantially extending the required time and effort compared to visible systems. In theory a ray tracing and characterization of each individual component of the optical system (mirrors, windows, and grating) should provide the transmission efficiency of the combined system. However, potentially unknown effects (contamination, misalignment, and measurement errors) can make the final error too large and unacceptable for most applications. Therefore, it is desirable to test and measure the optical properties of the whole system in vacuum and compare the overall response to the response of a calibrated photon detector. A proper comparison then allows the quantification of individual sources of uncertainty and ensures that the whole instrument performance is within acceptable tolerances or pinpoints which parts fail to meet requirements. Based on the experience with the IMAGE Spectrographic Imager, the Wide-band Imaging Camera, and the ICON Far Ultraviolet instruments, we discuss the steps and procedures for the proper radiometric sensitivity and passband calibration, spot size, imaging distortions, flatfield, and field of view determination.

Plain Language Summary As with all optical systems the calibration of wide-field ultraviolet (UV) systems includes three main areas: sensitivity, imaging quality, and imaging capability. The one thing that makes UV calibrations difficult is the need for working in vacuum substantially extending the required time and effort compared to visible systems. Based on the experience with the IMAGE Spectrographic Imager, the Wide-band Imaging Camera (WIC), and the ICON Far Ultraviolet instruments, we discuss the steps and procedures for the proper radiometric sensitivity and pass-band calibration, spot size, imaging distortions, flatfield, and field of view determination.

Key Points:
- Summary of tests for imaging capabilities and imaging quality of wide-angle UV instruments for space applications
- Description of steps to determine quantitative sensitivity of UV instrument
- Influence and test of environmental effects on imaging properties

Correspondence to:
H. U. Frey,
hfrey@ssl.berkeley.edu

Citation:
Frey, H. U., S. B. Mende, J. Loicq, and S. Habraken (2017), Calibration and testing of wide-field UV instruments, *J. Geophys. Res. Space Physics*, *122*, 6907–6921, doi:10.1002/2016JA022700.

Received 14 MAR 2016
Accepted 16 MAY 2017
Accepted article online 18 MAY 2017
Published online 15 JUN 2017

1. Introduction

Ultraviolet (UV) instruments for Heliophysics are mostly used to either observe the solar disk or corona or for observations of aurora and airglow on Earth or Mars [*Mende*, 2016a]. All these objects are close enough and extended in size that most of the time wide fields of view are desirable (several degrees per side) in order to observe larger portions of those objects simultaneously or a particular region over a longer time (many minutes) even if the observing platform moves. This is different from astronomical space telescopes that tend to have small fields of view like the Hubble Space Telescope's new advanced camera with a square field of view of about 0.06° per side [*Avila et al.*, 2016]. The particular challenge for the ground-based calibration and test of wide-field UV instruments are the difficulties to illuminate large portions of the detector simultaneously. However, it is an old wisdom that any scientific measurement is only as good as the quality of the instrument, and the quality of the instrument is determined by a careful calibration [*Mende*, 2016b].

One notable difference between visible and UV instrumentation is the difference in detector technology and characteristics for the detection of UV photons. Very often photon fluxes in the UV are very low and require intensification for an efficient detection. The image intensification devices then determine how sharp an object can be imaged, what a dynamic range from very low to higher photon fluxes can be recorded, and how well the quantitative relationship between the measured signal and the incoming photon flux can be established.

UV detector systems for 2-D imaging very often use a combination of a microchannel plate (MCP) coupled to the detector (CCD or complementary metal oxide semiconductor (CMOS)) by a fiber optic in order to enhance (intensify) the contrast in the final images. An MCP is an electron multiplier with a photocathode on the input side where an incoming photon creates one free electron. This free electron is then accelerated in the MCP and multiplied 10^4–10^8 times to create an electron cloud at the output. MCP assemblies for 2-D imaging use

different readout devices, either a position-sensitive multianode that provides an electric output signal corresponding to the input position or a phosphor screen where the electron cloud creates a bright light flash that can be recorded by the optical imaging device [*Werner*, 2010]. The combination of MCP pore size, phosphor screen to anode gap, potentially fiber optical reduction factor, and detector pixel size then determines the achievable spatial resolution.

Finally, UV instrumentation is very sensitive to contamination. The UV photon wavelength is smaller than that of visible photons, and Rayleigh scattering by very small particles is very efficient. Furthermore, UV photons are much more easily absorbed by small quantities of any matter which substantially increases concerns about cleanliness during tests and avoidance of contamination.

Material selection, a clean environment, and continuous clean nitrogen purging during instrument construction and storage minimize contaminants that are carried into space inside the instrument. This minimizes the redistribution of such contaminants inside the instrument once in orbit. External contaminants carried up into space on other structures are effectively avoided by long wait periods before the opening of protective covers (doors). Contamination by spacecraft propellant can be reduced by careful design of the geometry between spacecraft exhaust and optical instrument openings. Repeated star calibrations of known UV stars provide an excellent way of monitoring all losses of sensitivity including those due to contamination. Rocket underflights with known ground-truth calibrated instruments [*Wieman et al.*, 2016] or the comparison to redundant, stowed, and rarely used filters are other ways of potentially monitoring contamination losses.

Over the years several UV calibration facilities have been described. The facilities at the Naval Research Laboratory that were used for the Special Sensor Ultraviolet Limb Imager instrument on the Defense Meteorological Satellite Program satellites are described in *Kalmanson et al.* [2002]. The facilities at the Beijing Institute of Technology [*Yan et al.*, 2010], at the Centre Spatial de Liège that were used for the Imager for Magnetopause-to-Aurora Global Exploration (IMAGE) Spectrographic Imager (SI) calibration [*Habraken et al.*, 1998], the facilities at the Southwest Research Institute that were used for several planetary UV spectrographs [*Davis et al.*, 2014], and the facilities at Padua for the Probing of Hermean Exosphere by Ultraviolet Spectroscopy spectrometer on the BepiColombo mission [*Corso et al.*, 2013] are just a few examples of the many similar facilities around the world that all share basically the same main components of light source, collimator, and vacuum test chamber with mechanical manipulator. They all share the same main purpose of ground calibration of space instrumentation operating in the ultraviolet. This paper summarizes our experience with the IMAGE Far Ultraviolet (FUV) and Ionospheric CONnection Explorer (ICON) FUV instrument tests and calibration and is based on a presentation at the Measurement Techniques in Solar and Space Physics conference in 2015.

2. Instrument Properties and Calibration Tasks

The UV calibration tasks for any optical instrument can be summarized in three major groups of tasks, the determination of the imaging capabilities, the imaging quality, and the quantitative sensitivity or photometric calibration (Table 1).

The most severe atmospheric absorption of UV photons by molecular oxygen occurs below 240 nm, while molecular nitrogen absorbs below 100 nm [*Rothman et al.*, 2009]. Therefore, the whole test assembly for UV instrumentation (from source to device) has to be under vacuum. Thus, testing and calibrating in the UV is much harder and more expensive than testing in the visible that can happen in air. A potential failure of not just the instrument but also some test equipment can require extensive troubleshooting and hours if not days of vacuum equipment time.

The general setup for UV instrument tests and calibration is shown in Figure 1. The instrument is placed inside a vacuum chamber on a manipulation stage that allows for at least two rotations along axes perpendicular to the incoming light beam plus potentially one or two horizontal translations. The two rotation axes need to intersect the instrument at the entrance aperture; otherwise, a rotation would shift the instrument aperture out of the incoming beam and a corresponding instrument translation would be needed to compensate for that. A suitable UV source like a commercial low-pressure gas discharge lamp with specific line emissions (Hg or Ne) or a commercial high-pressure gas discharge lamp for continuum emissions (hydrogen, deuterium, Ar, Xe) can provide the desired input photons that are then sent through a monochromator for the selection of

Table 1. Main Calibration Tasks for Wide-Field UV Instruments and Section Numbers Where They Will be Discussed in This Paper[a]

General property	Specific calibration task
Imaging capability	
	3.1 Aperture size
	3.1 Field of view
	3.2 Pointing accuracy, knowledge, and ***repeatability***
Imaging quality	
	3.3 Imaging geometric distortions
	3.4 Spot size or spatial resolution
	3.5 Flatfield or imaging homogeneity
Quantitative sensitivity	
	3.6 Passband
	3.7 Radiometric sensitivity
	3.8 Detector background
	3.9 Stray light background
	3.10 Linearity
	3.10 Dynamic range

[a]Properties that can be temperature-dependent are shown in bold italic letters.

the particular wavelength of interest. All UV instruments for Heliophysics applications look at objects at large distances that produce parallel wavefronts for the observer. Thus, during tests the divergent beam of the test equipment has to be transformed into a collimated small diameter beam of parallel light in order to mimic this condition. Often a filter wheel with pinholes of different diameter or with windows like MgF_2 (cutoff 110 nm) or BaF_2 (cutoff 135 nm) is used to either reduce the beam intensity or eliminate specific wavelengths, respectively. A calibrated photomultiplier tube (PMT) with a known response of output current relative to input photon flux monitors the light flux from the source for the final quantitative transformation. For thermal testing the instrument has to be surrounded by heating/cooling panels that can be controlled for temperature range and stability. All this equipment has to be either inside the thermal vacuum test chamber or connected to it through vacuum tubes.

3. Calibration Steps

The UV instrument test and calibration are a multistep process by which the instrument properties are ideally determined individually. Most of the time it is not sufficient to only determine the end-to-end throughput and uncertainty of the whole instrument. It is better to develop calibration procedures that allow quantifying the various parameters in Table 1 separately. That way not only are the individual contributions to the overall uncertainty quantified, but they can also potentially be individually corrected if time and cost permit.

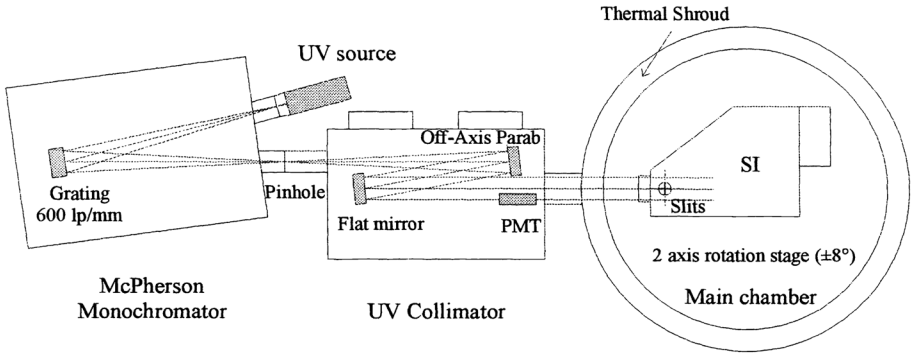

Figure 1. Setup for the test and calibration of the IMAGE-SI instrument that is typical for wide-angle UV instrument calibration. This particular setup inside the main chamber included two perpendicular rotational capabilities with rotation centers at the instrument aperture (entrance slits), the so-called Mechanical Ground Support Equipment (MGSE), to scan all directions through the whole field of view. The source, monochromator, and collimator that are vacuum connected to the main chamber constitute the Optical Ground Support Equipment (OGSE).

3.1. Aperture Size and Field of View

The aperture size determines how much light can enter the instrument. It thus affects the overall radiometric sensitivity (section 3.7). Most of the time it is known from the manufacturing, but it can also be measured by microscopy or laser metrology.

The field of view (FOV) of an optical instrument is primarily determined by the size and shape of the entrance aperture, the total view angle through that aperture, and any potentially beam size limiting elements inside of the instrument like mirror or grating masks, window holding fixtures, and even unwanted restrictions from misaligned baffles. The size and shape of the FOV can be determined in the laboratory setup when the instrument is rotated with respect to the incoming parallel light beam until the signal drops off, thus marking the edge of the field of view. This dropoff can be sharp for imaging instruments with good spatial resolution and baffling but can also be more gradual for spatially integrating instruments or especially single-pixel photodiodes. Limiting factors for the accuracy of this measurement are the size of the incoming beam and the accuracy and repeatability of the rotation stages.

The measurement of the FOV has to be related to two instrument reference frames, one centered at the detector and the other at the entrance aperture. These reference frames may be rotated with respect to each other, and thus, an additional measurement of a fiducial like a reference optical cube at the outside of the instrument body has to be performed to establish the relative orientation between the two reference frames [*Habraken et al.*, 1999]. This requirement will be discussed in section 3.2. After the instrument integration to the spacecraft the relative orientation of the instrument reference frame with respect to the spacecraft body has to be determined. A direct instrument FOV measurement with the whole observatory in a large enough vacuum chamber is often prohibited by cost and time constraints. Thus, this relationship is most of the time established between the instrument reference optical cube and a spacecraft reference cube by theodolite autocollimation or similar techniques [*Hetherington et al.*, 2013].

Imaging instruments have the big advantage that their field of view can be confirmed after launch on orbit. The positions of stars are known to better than arcsecond accuracy, and pointing the instrument to a star field with enough stars of sufficient brightness (depending on instrument sensitivity) can yield a very accurate determination of the size and shape of the field of view.

Integrating instruments (like photometers) have to be carefully characterized on the ground as the verification of their exact field of view is more difficult to make on orbit. A bright UV source (Sun or Moon) can get scanned across the FOV and the response then deconvoluted with the angular extent of the source [*Hock et al.*, 2012]. Given sufficient sensitivity smaller sources (Jupiter or B-class UV stars) can be used too [*Morrison et al.*, 2002], but often their UV fluxes may not be sufficient.

3.2. Pointing Accuracy, Knowledge, and Repeatability

The pointing of the center line of sight of the instrument is determined with respect to alignment cubes on the instrument body. In the case of ICON FUV the instrument was placed on a tip/tilt and rotation stage. This Mechanical Ground Support Equipment (MGSE) provided the ability to rotate the instrument around the entrance pupil. The rotation range covered more than the entire FOV (24° vertical, 18° horizontal). The manipulator is composed of three linear actuators (tripod) on which a rotation table is placed through a kinetic mount support.

Before manipulating the flight instrument in vacuum a dummy mass has been placed on the manipulator to characterize and simulate the motion range, accuracy, and repeatability of the manipulator in easier air conditions. The dummy mass was used to completely characterize the MGSE independent of the instrument and isolate MGSE-induced uncertainties from instrument-induced uncertainties. A metal strip simulated the entrance pupil of the instrument. The light beam was then adjusted in such a way that the optical axis passes through the rotation axis of the main rotation stage. A reference optical cube was placed on the outside of the dummy mass so that all MGSE motions could be characterized with the aid of a laser tracker and theodolites. The absolute accuracy and repeatability of the manipulator was 3 arcsec. The incoming light beam and the optical portion of the test equipment, the Optical Ground Support Equipment (OGSE), have thus been characterized and referenced with the MGSE for all the testing under vacuum.

The setup is used not only during ambient temperature tests but also during thermal vacuum testing in order to characterize the response to external temperature variations. As a first step the thermal behavior of the test

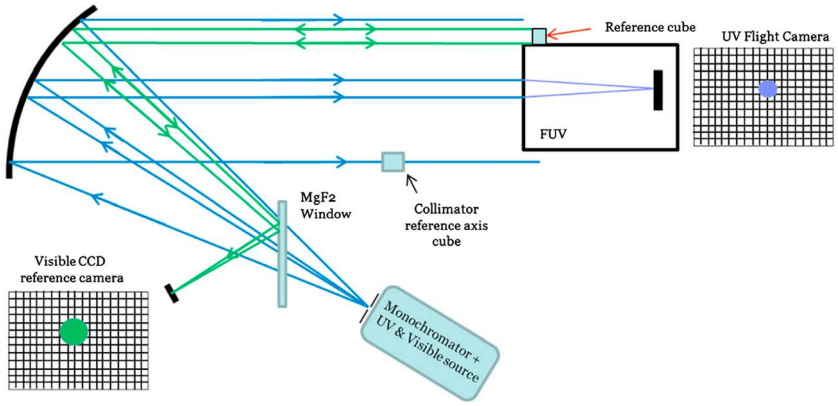

Figure 2. Overall setup for the alignment of the ICON FUV instrument. The measurement process is described in the text.

environment has to be characterized so that it can later be separated from the thermal response of the device under test. The control of the line of sight during thermal cycles is enabled with a reference mirror cube placed on the instrument body and an autocollimation process with a reference CCD camera (Figures 2 and 3). Light reflected by the reference cube returns back into the collimator and is focused into the reference camera. The comparison of the reflected beam imaged onto the reference camera as a function of the different angles and temperatures gives the ability to realign the instrument and compensate for misalignments due to the thermo-mechanical constraints of the MGSE structure. Any remaining shifts of beam positions in the UV instrument for different temperatures are then a result of thermal effects on the instrument structure. The angular resolution of the reference camera and the accuracy and repeatability of the mechanical stage (3 arcsec) have to be better than the angular resolution of the instrument (for ICON FUV 3 arcmin) in order for this procedure to provide reliable results. Later the alignment with respect to the spacecraft structure is determined by theodolites looking at the instrument alignment cube and alignment cubes on the spacecraft structure.

3.3. Imaging Distortions

All imaging instruments suffer from some degree of optical distortions (optical aberration). These deviations from a rectilinear projection are often due to the properties and/or manufacturing uncertainties of their optical elements but can also simply be the result of limitations in manufacturability within budget constraints. The most commonly known distortion is barrel distortion with straight lines bulging outward with increasing

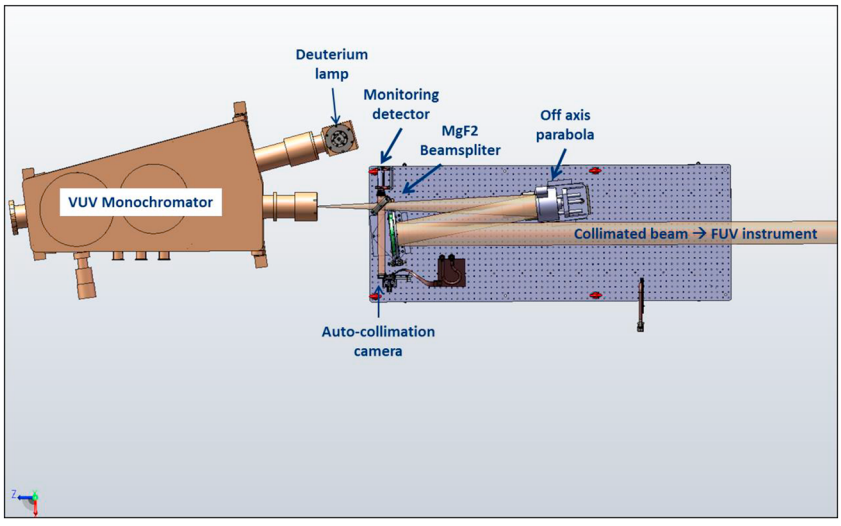

Figure 3. Setup for the external portion of the ICON FUV alignment. All this equipment is under vacuum and connected to the test chamber through vacuum tubes.

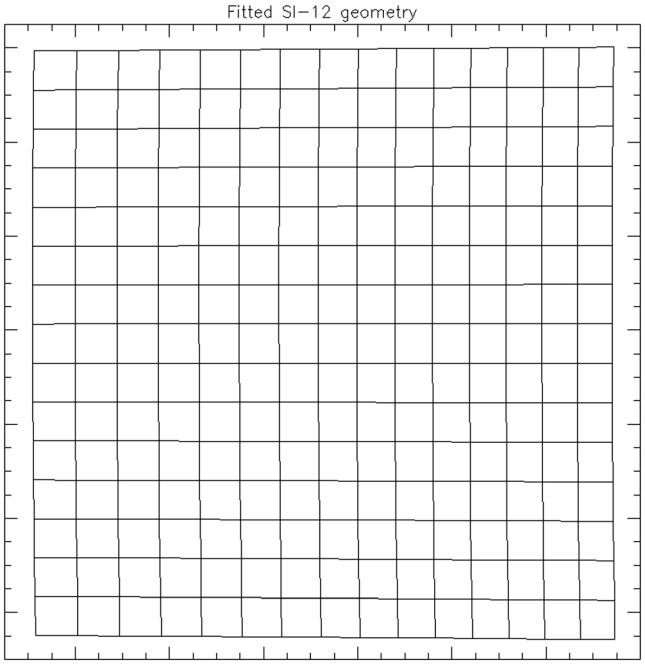

Figure 4. Fitted position of measurement points in horizontal and vertical angles on the IMAGE Spectrographic Imager SI-12 channel detector showing a small tendency to (left) barrel and (right) pincushion distortion in the horizontal direction and pincushion distortion in the vertical direction. A rectilinear projection would maintain straight lines.

distance from the optical axis. Another distortion is the pincushion distortion where lines bulge inward with increasing distance from the optical axis or a mix of both called mustache distortion. Very often imaging distortions are determined together with field of view measurements using a narrow beam of light. When the instrument is rotated horizontally/vertically (tip/tilt) by fixed angular steps, the relative position of the resulting spot is determined and compared to expected positions in pixel space. Figure 4 shows an example from the IMAGE Spectrographic Imager calibration. The magnitude of distortions for the SI can be seen in the horizontal direction and much less so in the vertical direction.

From a sufficient number of measurements (generally >20) a distortion function or table can be constructed by least squares fitting the measured pixel positions and offset angles. For IMAGE SI a polynomial of the form

$$X' = a[0] + a[1]^{*}x + a[2]^{*}y + a[3]^{*}x^{*}y + a[4]^{*}x^{*}x + a[5]^{*}y^{*}y \quad (1)$$

$$Y' = b[0] + b[1]^{*}x + b[2]^{*}y + b[3]^{*}x^{*}y + b[4]^{*}x^{*}x + b[5]^{*}y^{*}y \quad (2)$$

was used with X' and Y' as the measured horizontal and vertical pixel positions, x and y as the offset angles, and parameters a and b as the least squares fitted optimization parameters.

Optical ray tracing can guide the decision as to how many measurements and how many fitting parameters will be required for an optimum solution of equations (1) and (2). The short-wave channel of the ICON FUV instrument for instance shows a much more complicated geometric distortion pattern [*Loicq et al.*, 2016] where the rectangular field of view is distorted into a banana-like shape. For this instrument it was decided that the qualitatively larger and more complicated distortion required more measurements (>70) and a mix of polynomials and trigonometric functions that provided a better overall fit with smaller residual errors [*Mende et al.*, 2017].

During thermal testing of IMAGE SI it was discovered that the position of spots changed slightly with temperature. The spots did not move all into the same direction, which would have preserved the distortion but shifted the optical axis. Instead, it appears that the distortion itself changed. The most likely cause of such a shift is the thermal expansion or contraction of optical element fixtures that are not completely temperature compensated in the mechanical design of the system. The variation, however, was smaller than one final science pixel and therefore considered as acceptable (Figure 5).

3.4. Spot Size or Resolution

The response of an imaging system to a beam of parallel light determines the size of an imaged spot. If for instance a single star is brought into best focus of an imaging system then the point spread function (PSF) describes the response to this point source. In imaging systems the PSF is often modeled by a two-dimensional Gaussian distribution and the full width at half maximum (FWHM) describes the size of the spot. Calculation of the encircled energy within the spot gives then the energy distribution of the PSF. Design guidelines very often require that 50%, 80%, or 90% of the incoming energy should be concentrated

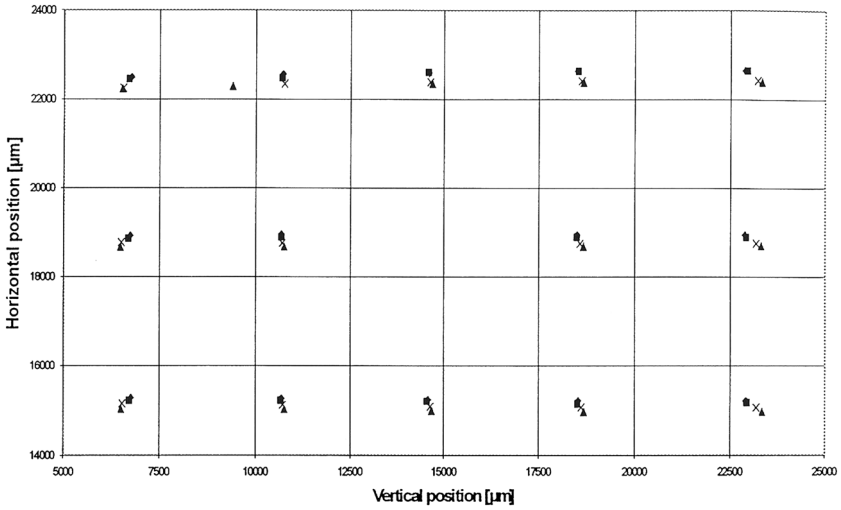

Figure 5. Variation of the spot position with temperature for the SI-12 channel of IMAGE FUV. The same fields were measured at −20° C (black diamond), −10° C (black square), +40°C (black triangle), and room temperature (cross). A physical pixel is 140 µm. Note the different horizontal and vertical scales.

within a certain number of final science pixels (most often 2 × 2 pixels [see, e.g., *Howell*, 2006]). The setup in Figure 1 is used with a small pinhole, and the size of the resulting spot is determined in the horizontal and vertical directions to test the imaging quality with respect to the requirement. It is important to verify the spot size not just in the center of the field of view but also at the extreme fields. For most optical systems the plane of best focus is curved and so a planar detector will sample a range of spot sizes depending on the curvature of the best focus and the size, alignment, and orientation of the detector. This is the reason why the detector of the IMAGE Wide-band Imaging Camera (WIC) was curved to accommodate the focal surface of the concentric optics [*Mende et al.*, 2000a]. Furthermore, slight misalignments of mirrors will also represent themselves as increased spot sizes toward the extreme field angles.

The test setup has to be carefully designed. The pinhole has to be placed at the focus of the collimator. Finally, a size has to be used that after applying the appropriate magnification, the ideal image of the pinhole at the detector should be significantly smaller than the physical size of a pixel. Otherwise, the test will examine the size of the pinhole image and not the optical properties of the instrument. The divergence of the beam was measured before the tests with the flight system using a photomultiplier tube and a movable sharp edge. The resulting spot size is the combination of the divergence of the collimated beam (1 arcmin for the setup in Figure 1 during the IMAGE SI calibration) and the optical resolution of the instrument (7 arcmin for IMAGE SI) [*Habraken et al.*, 1998]. An example of spot size measurements for the IMAGE SI is given in Figure 6.

3.5. Flat Field or Imaging Homogeneity

An ideal imaging system will respond to a homogeneous illumination with an absolutely uniform response. However, there are three major contributions to deviations from a uniform response: (1) vignetting and obscuration, (2) variations in dark signal, and (3) pixel-to-pixel variations in sensitivity. The first is the variation of illumination due to the optical design when vignetting and obscuration in the light path can limit the photon flux to some regions of the detector, most of the time the outer portions. Later in this section we will discuss a case where the central region of the image is mostly affected. These variations are typically slow across the field of view. The variability of the detector background (dark current) will be discussed in section 3.8. Another effect is the pixel-to-pixel variation in sensitivity across the detector that is usually due to processing steps during detector manufacture.Any nonuniformity of a 2-D detector response to a homogeneous illumination has to be corrected by flatfielding with

$$C = \frac{(R - D)\cdot m}{(F - D)} \tag{3}$$

with the corrected image C, the raw image R, the dark image D, the flat-field image F, and the average value $m = <F - D>$ over the whole detector. While all capital letters denote 2-D images the small letter m is a

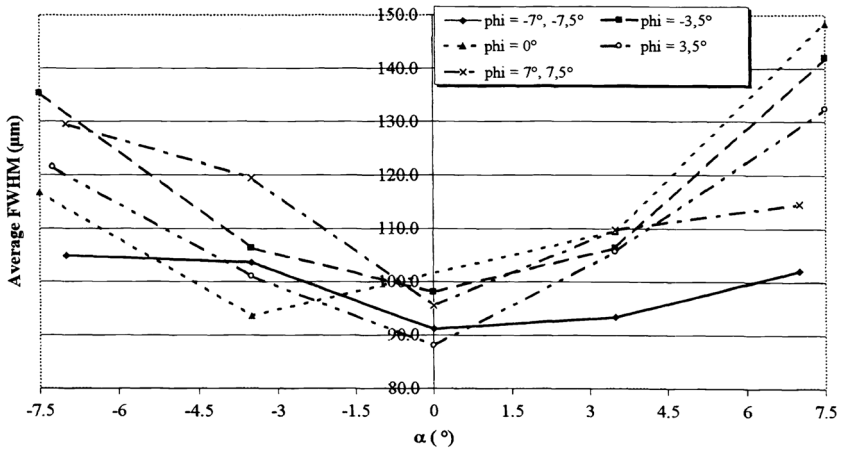

Figure 6. Spot size full width at half maximum (FWHM) in micrometer for different fields in the SI-13 channel of the IMAGE SI. The angle α goes horizontally across the detector, while the angle phi refers to different vertical angles. The physical pixel size was 140 µm on the 18 × 18 mm^2 detector (from *Mende et al.* [2000b] reproduced with permission).

scalar. The flat-field correction has to be performed on a pixel-by-pixel basis, and the end result is a uniform image when illuminated by a uniform light source. This measurement can be accomplished outside of the vacuum chamber when only gain variations of the detector are considered. Very often it is advantageous to rotate the detector with respect to the fixed light source to clearly separate source inhomogeneity from detector nonuniformities. Illuminating the detector with diffuse but homogeneous light and recording the detector response should be done many times, and the average response will provide the flat-field image. Counting statistics show a Poissonian distribution where the standard deviation of the counts can often be estimated by the square root of the counts. In a full characterization of the detector system a series of repeated measurements should be performed to determine the standard deviation of the response and deviations from the square root can be attributed to the pixel-to-pixel variability.

In many optical systems the flatfield is not only determined by the detector alone but also affected by optical vignetting and dust or scratches on mirrors or windows and the full instrument should be characterized. A homogeneously illuminated white object at close range (out of focus) can be used in many cases [see, e.g., *Howell*, 2006].

The IMAGE SI had a paraxial Wadsworth configuration [*Mende et al.*, 2000b], and one of the disadvantages was the need for a hole in the grating through which the light entered the spectrographic portion of the instrument. This arrangement produced a blind region in the center of the image and would have been unfeasible for any staring observation of the aurora or night sky. However, as the IMAGE satellite was spinning this blind region swept over the target and the missing part of the image was filled during each spin by the time delay integration (TDI). Figure 7 shows an image of the grating as seen by the detector and clearly shows the dark or blind central region of the image. The spin of the satellite swept this blind region horizontally across the scene and generated a strong flatfield variation in the vertical direction (Figure 7, right). During quantitative analysis of these IMAGE SI images the flatfield corrected for this ~30% loss in sensitivity in the central part of the final images.

The pixel-to-pixel response can have substantial wavelength dependence. Most of the time that dependence is caused by variations in the coating properties of the optical elements (thickness or chemical composition). A complete characterization of the instrument should measure the wavelength dependence for several fields.

It is highly desirable to determine the flatfield again on orbit after launch. For instance nonuniform contamination during launch and early on-orbit outgassing could create variations from the ground test results. A standard UV star can be imaged in different fields, and the stacked-up images could provide a quasi-uniform average image. The maneuverability of the ICON spacecraft will allow us to point the ICON FUV to nadir at the subsolar point, and the featureless UV dayglow will provide a uniform illumination to determine the flatfield.

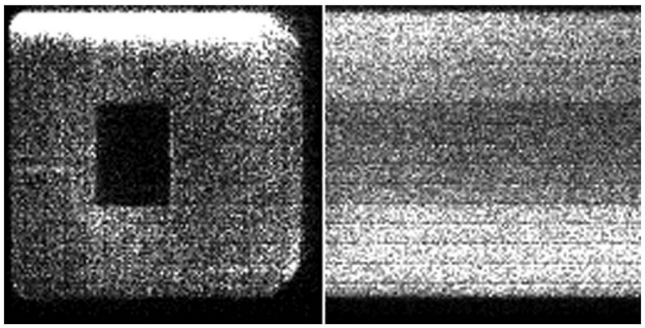

Figure 7. (left) Image of the IMAGE-SI grating and (right) resulting flatfield variation during the integration on the rotating satellite and with TDI implemented. The bright region at the top of the left image comes from a light leak that was fixed before the right image was taken.

3.6. Spectral Passband or Instrument Transmission

Careful characterization of the spectral passband is important to understand the shape of the transmission function and to determine potential contributions from nearby lines or line blends. It is especially important for wideband instruments that will record several spectral lines like in auroral observations. The IMAGE Spectrographic Imager SI-12 channel was tuned to 121.8 nm in order to see the Doppler-shifted component of hydrogen Lyman-alpha emission from precipitating energetic protons [*Mende et al.*, 2000b]. At the same time, it had to suppress the approximately 100 times brighter Lyman-alpha emission from the geocorona that is emitted at the rest wavelength of 121.567 nm [*Mende*, 2016a]. This was achieved by using an entrance slit grille with nine individual slits instead of only one and a similar exit slit grille which was specifically displaced to block the rest wavelength Lyman alpha and allow the Doppler-shifted component to pass through. This combination of entrance and exit slit grills created a periodic passband with high contrast, which had to be confirmed and characterized over the wavelength range of 117–127 nm (Figure 8).

The IMAGE-SI-12 transmission was determined in the vacuum chamber using an argon-filled lamp and a monochromator with a resolution set to 0.2 nm. The exit slit of the monochromator was coupled to the collimator which produced a collimated beam of light entering the instrument. The output of the monochromator was regularly sampled by a calibrated photomultiplier tube (PMT) which could be moved into and out of the beam. The PMT measured the absolute photon flux which was then compared to the measured SI detector signal.

The IMAGE-SI-13 channel (Figure 9) was primarily tuned to detect the 135.6 nm emission from atomic oxygen. However, there are several weaker emissions of the nitrogen N_2-Lyman-Birge-Hopfield (LBH) band close by that add to the pure oxygen signal. Theoretical modeling with a standard atmosphere and different auroral electron energy distributions determined that low-energy auroral electrons ($<$1 keV) generate 10 times more 135.6 nm photons than nitrogen LBH emissions in the 131–140 nm range of the SI-13 passband. However, at higher energies ($>$10 keV) the LBH emissions are about 2 times stronger than the oxygen emission. The quantitative analysis of images has to take this variability into account to come up with realistic auroral energy fluxes when a mean electron energy can either be determined from other sources (in situ measurements by low-altitude satellites like FAST) or estimated from ground-based radar measurements [*Frey et al.*, 2003]. If such mean energies cannot be independently determined then the theoretical modeling provides the range of potential errors for the quantitative analysis.

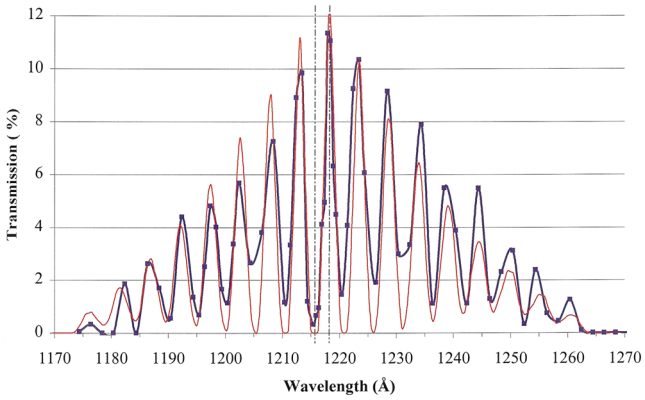

Figure 8. Transmission of the IMAGE-FUV-SI-12 channel as a function of wavelength. The red line is the theoretical profile, and the black line is a fit to the measurement points (black squares). The vertical line at 121.56 nm marks the rest wavelength of hydrogen Lyman alpha. Around the target wavelength of 121.8 nm (second vertical line) the measurement step size was 0.05 nm, while it was 0.2 nm elsewhere.

A full instrument characterization should also include a measurement of the passband temperature dependence. Some optical materials (for instance salts)

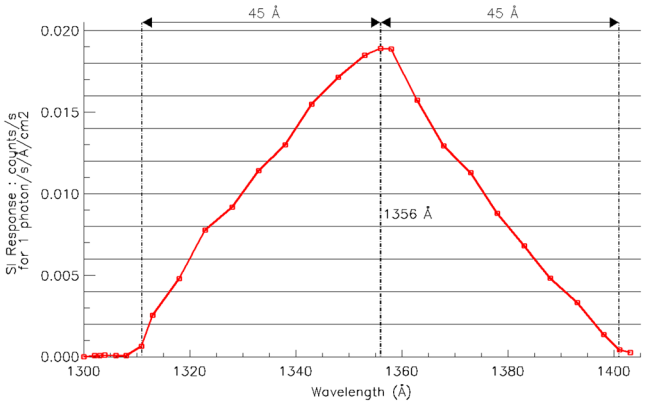

Figure 9. Transmission of the IMAGE-FUV-SI-13 channel as a function of wavelength.

show a strong temperature dependence of their transmission. They can be used to eliminate unwanted emissions (for instance, 130.4 nm if 135.6 nm is the target) by carefully controlling their temperature [*Mende*, 2016b]. However, a band-pass shift can also occur during uncontrolled temperature changes of the instrument and such temperature dependence has to be measured in a controlled manner on the ground.

3.7. Radiometric Sensitivity

The response C (in counts per second per pixel) of an optical instrument can be described by

$$\boldsymbol{C} = \boldsymbol{f}(\lambda)\cdot\boldsymbol{A}\cdot[\,\boldsymbol{T}(\lambda)\cdot\boldsymbol{E}(\lambda)\cdot\boldsymbol{\Omega}\,] = \boldsymbol{f}(\lambda)\cdot\boldsymbol{A}\cdot\boldsymbol{D}(\lambda) \tag{4}$$

with the wavelength-dependent photon flux $f(\lambda)$ at the entrance aperture (in photons per square centimeter per second per steradian), the entrance aperture size A (in square centimeter), the transmission efficiency from the entrance aperture to the detector $T(\lambda)$ (dimensionless), the quantum efficiency of the detector $E(\lambda)$ (in counts per incident photon), and the solid angle of an individual pixel Ω (in steradian). The entrance aperture is mostly determined by the instrument design and should be known to within manufacturing accuracy. The transmission, quantum efficiency, and pixel solid angle can be measured individually, but most of the time the calibration process determines them together as an overall detection efficiency $D(\lambda)$. Both the instrument transmission T and detector quantum efficiency E are wavelength-dependent, thus making the detection efficiency $D(\lambda)$ also wavelength-dependent.

The convolution of the instrument transmission with the detector quantum efficiency determines the overall radiometric sensitivity of the instrument. The most commonly used photocathode materials in the far ultraviolet (for instance CsI or KBr) have strongly wavelength-dependent quantum efficiencies (QE) between 30% and 5% from low to high wavelengths [see, e.g., *Larruquert et al.*, 2002]. In principle, the radiometric sensitivity of an instrument could be calculated if the transmission and QE are measured independently. However it is advisable to characterize the whole instrument by using a setup similar to Figure 1. A calibrated photomultiplier tube characterizes the input beam and measures the number of photons hitting the instrument per second and square centimeter. A single-photon detector will then measure the instrument response as events per second which then gives the radiometric sensitivity at the specified wavelength.

At low-photon flux individual photons can be recorded with intensified systems (see section 1) in the so-called photon-counting mode. The electric output can either be measured by a position-sensitive multianode, or the apparent brightness of each bright flash on the phosphor screen can be recorded by CCD or CMOS detectors. The plot of how often a specific brightness was recorded as a function of brightness level is called pulse height distribution.

The pulse height distribution of the intensified-detector system has to be determined, and the average can be used to determine the real output signal in events per second for a fixed input photon flux. The pulse height distribution strongly depends on the applied high voltage and has to be determined for the whole expected high-voltage range. Figure 10 shows the pulse height distribution for a fixed MCP high voltage (1050 V) on IMAGE WIC. For that high voltage each detected photon created a well detectable bright scintillation in a single CCD image of 30 ms integration. Using a low-photon flux where individual events did not interfere with each other either in time or in pixel space each event could be analyzed and the total analog-digital units for each individual event could be determined. The final histogram in Figure 10 shows the mean size of a photoelectron scintillation is 100 CCD A-D units.

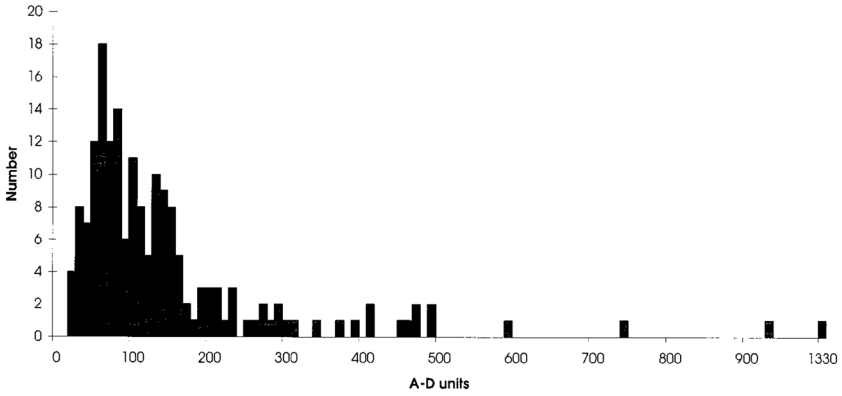

Figure 10. IMAGE WIC pulse height distribution in CCD digitization units (from *Mende et al.* [2000b] reproduced with permission).

3.8. Detector Background

The most common detector background in modern imaging systems comes from the CCD dark current. It is due to thermal energy and created by the random generation of electrons and holes within the depletion region of photosensitive devices. The electron/hole pairs generate a relatively small electric current even when no photons hit the device. The dark current is temperature-dependent and can be reduced by cooling of the CCD [see, e.g., *Howell*, 2006]. For a fixed temperature the dark current creates a constant average offset, but because the charge generation has a Poisson distribution it also creates a randomly varying noise contribution in addition to a potential pixel-to-pixel variation of the noise background. Examples of temperature dependences of CCD dark currents can be found for instance in *Widenhorn et al.* [2002] and *Kameda et al.* [2016].

As the dark current does not depend on the incoming photon flux it can be determined outside of the vacuum chamber. The two main CCD architectures, interline transfer and frame transfer, create different dark current backgrounds. While an interline transfer CCD has an almost constant background the frame transfer CCD has a varying background in the direction of frame transfer (Figure 11). In an interline transfer CCD each active pixel has a storage area next to it, and at the end of an integration the charge of every pixel is shifted into its storage area before readout. A frame transfer CCD has a duplicate storage area below the active sensor area which is masked so no light can reach it. At the end of the integration the whole image is quickly shifted into the storage area so it cannot accumulate more electrons from light illumination. After this transfer period of several microseconds the image is read out line by line during the readout period which determines the minimum integration time and is on the order of several milliseconds. The last lines to be read out continue to accumulate dark current and appear slightly brighter than the first lines that are read. The image in Figure 11 is the sum of 100 frames of 120 ms integration each plus 100 readout times, and therefore, the relative variation of the

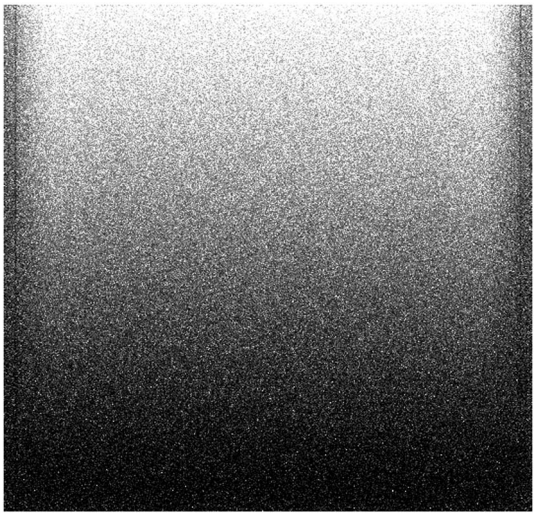

Figure 11. Dark image of the ICON FUV short-wave channel. The image is the sum of 100 frames of 120 ms integration each. The contrast of this image is strongly enhanced to show the variation of the dark current background from the bottom to the top of this summed image (19,400 A/D units to 21,500 A/D). The detector is the 1 M Frame Transfer CCD Image Sensor FTT1010M from DALSA Professional Imaging.

background from the bottom to the top is more pronounced than it would be for a single readout after a 12 s integration.

Figure 11 also shows the fine-scale variation of the background due to the combination of readout noise, dark signal Poisson noise, and pixel-to-pixel variations in dark signal. The read noise of a system represents the error that is introduced during the quantification of the electronic signal on the CCD. The charge from each pixel in a CCD is transferred through a single readout system where the charge is converted to voltage and then amplified prior to the digitization. The on-chip preamplifier introduces a noise source as a specific amount of charge is not always transformed into exactly the same voltage. This readout noise is typically expressed as the root-mean-square of number of electrons that every pixel will show. While the background from dark current can easily be determined and subtracted from images the readout noise cannot be removed in an exact manner. But as long as it shows a Gaussian distribution it can be treated in a statistical manner during quantitative analysis of images.

CCD devices are generally operated with an artificially induced electronic offset (bias level) in order to ensure that the analog-to-digital converter at its output always receives a positive input signal. The bias is generally a constant offset, but it can vary with temperature if the electronic circuits are not well designed. The bias level can be monitored by reading certain regions (over-scan region at the side of CCD chips) without moving any charge or by reading an image with zero exposure time. However, one can consider the bias level as part of the dark signal and remove both components together in the final image processing.

3.9. Stray Light Background

The stray light background can come from different sources: (1) out of passband light entering the instrument through the entrance aperture, (2) in-band light from outside of the FOV scattered inside the baffle, (3) light from other diffraction orders that could reach the detector (if a diffraction grating is used), (4) zero-order reflection within the instrument, (5) light scattered within the instrument, (6) light entering the instrument through unwanted paths (venting holes), and (7) in-field in-band scatter.

The out-of-band stray light contribution (a) can be tested at the same time as the instrument transmission is measured (section 3.6) by shining off-band light into the aperture. If present it will represent itself as a fuzzy increase of the overall signal when compared to the true dark current response and depending on the spectral suppression properties should be well below 1% or even lower for grating based instruments.

The stray light background (b) is a bit difficult to measure. An intense beam of in-band UV light is required to illuminate the instrument from outside of the science FOV but in a way that there are no reflections from vacuum chamber structures like the tank walls or the instrument mounting structure that could cause spurious effects. These structures will not exist in-flight, and any scattered contribution from those structures would be false positive signals. Spacecraft structures on the other hand could scatter light into the instrument on orbit but will in most cases not be available at the time of instrument level testing on the ground.

The contribution (c) can be directly measured since monochromatic light will generate easily separable multi-order signals. However, we should note that this contribution only affects systems with diffracting elements.

The contributions of stray light sources (d–f) cannot be tested effectively but should rather be investigated by ray tracing and be reduced by design features like baffling vanes, black anodization of all internal surfaces, and the use of optical surfaces with low scattering levels (RMS roughness better than 10 Å [*Habraken et al.*, 1997]).

In-field in-band scatter can compromise the ability to obtain sharp contrast images because it creates a halo of stray light around bright objects within the field of view [*Peterson*, 2004]. It can be determined with a knife-edge test where a sharp boundary (slit) is placed at the focus of the collimator. One can then determine how the scattered light falls off at the edge of the boundary.

3.10. Linearity and Dynamic Range

The dynamic range of a CCD chip is generally defined as the full-well capacity (largest amount of charge a pixel can store before the start of saturation) divided by the camera noise. It describes the ability of a camera to simultaneously record very low light signals alongside very bright signals [see, e.g., *Howell*, 2006].

The ratio can either be expressed in decibels (20 times the logarithm of the ratio of full-well capacity to read noise in order to convert amplitude to power) or alternatively as the equivalent number of A/D units (bits) that are required to digitize the signal. When the charge collected in a single CCD pixel exceeds the saturation level of the device that charge may begin to fill adjacent pixels. This so-called blooming contaminates the signal of the adjacent pixels. It causes the device to deviate from a linear response to different levels of illumination, and as a result the quantitative performance of the camera is compromised. The behavior of the system has to be tested with increasing photon fluxes (different pinhole diameters or opening of monochromator slits) until input and output are no longer linearly proportional to each other.

Photon counting detectors are count rate limited because it takes a finite response time for a single event to be analyzed (dead time). If a second event arrives during that dead time it will either be ignored or in some instances it can pile up on the first event. In both cases the second event will not be counted. The position-sensitive cross-delay line (XDL) detectors on the IMAGE SI had a maximum system count rate of 10^5 c/s and a single pore rate of 1 c/s [*Mende et al.*, 2000c]. Modern systems with faster electronic can process more than $2 \cdot 10^5$ c/s and more than 100 events per second per resolution element [*Vallerga and Siegmund*, 2000] but can still get overwhelmed if small areas receive large photon fluxes from bright objects. The XDL detector linearity and dynamic range can be tested with electronic stimulation pulses of different known frequency C and then the dead time constant t can be determined from the detected count rate D using

$$\boldsymbol{D} = \frac{\boldsymbol{C}}{1 + \boldsymbol{C}\cdot\boldsymbol{t}} \tag{5}$$

4. Testing of UV Instrument in Air

The full functional testing of UV instruments has to be done in a vacuum environment with ultraviolet light of the correct wavelength. There is one notable exception where some testing can be done in air using visible light. In an all-reflective system most of the reflective optical properties are independent of the particular wavelength of the light. The law of reflection still applies that the angle of incidence equals the angle of reflection. The reflectance can be, and in most cases is, different at different wavelengths as well as refractive and diffractive properties. For a reflective diffraction grating the grating equation

$$\boldsymbol{d}\cdot[\sin(\boldsymbol{\theta_i}) + \sin(\boldsymbol{\theta_m})] = \boldsymbol{m}\cdot\boldsymbol{\lambda} \tag{6}$$

still holds where for a specific grating spacing d, wavelength λ, incidence angle θ_i, and integer numbers m, intensity maxima occur at specific output angles θ_m. It is easy to see that

$$\sin(\boldsymbol{\theta_m}) = \boldsymbol{m}\cdot\frac{\boldsymbol{\lambda}\cdot\boldsymbol{a}}{\boldsymbol{d}\cdot\boldsymbol{a}} - \sin(\boldsymbol{\theta_i}) \tag{7}$$

and the angle θ_m is the same for any multiplication of λ and d with the same factor a. So a particular diffraction grating with spacing d will diffract light of 140 nm (FUV) into exactly the same direction as a grating with spacing $4{\cdot}d$ will diffract light of $4{\cdot}\lambda$, or in this example visible light of 560 nm. If the detector system is replaced by a detector that is sensitive to the other wavelength that property will allow for the full testing of the optical portion of a UV instrument with visible light. However, if there are any transmissive elements in the optical path (like a MgF_2 window for the FUV detector) their properties have to be matched or compensated by appropriate materials for visible light, like a quartz window of specific thickness.

This property of reflective systems was used during the initial testing of the ICON FUV instrument to verify the alignment of the optical mirrors, grating, and photon detector. The target wavelengths for ICON FUV are 135.6 and 157 nm. By using a 900 lines per millimeter visible grating instead of the 3600 lines per millimeter UV flight-grating all the optical tests could be done with 542.4 and 628 nm visible light in a clean air environment instead of inside a vacuum. The MCP-taper-CCD detector system of the FUV instrument was replaced by a visible camera (Atik 11000). This test provided a first approach to get all the orientations and distances between optical elements correct. But it had to be repeated, verified, and potentially corrected with the final flight UV instrument and UV light under vacuum.

5. Testing Environment

As mentioned earlier, atmospheric absorption requires a test environment under vacuum. But the vacuum environment is also advisable for contamination avoidance. The two most severe contamination concerns are thin layers of organic compounds and particles [*Schühle*, 2003]. Outgassing organic materials from the instrument, test equipment, or spacecraft (from tapes, adhesives, and cables) can create molecular contamination and absorb UV photons before they reach the detector. Particles can cause photon scatter and thus reduce the photon flux at the detector. The most important preventive steps to avoid contamination are careful cleaning of all hardware, design of the instrument without potential contamination sources (clamping instead of gluing), protective devices (door), handling in a cleanroom and during transport, purging with clean gas, potential active trapping (zeolite absorbers), and continuous monitoring (quartz crystal microbalance and witness samples). All satellite missions with UV instrumentation adopt contamination control plans early during the development in order to reduce or avoid contamination during the whole project from manufacturing through in-orbit science operations.

6. Conclusions

The quantitative calibration of a wide-field UV instrument is a complex process with many individual tasks to fully characterize the imaging capabilities, imaging quality, and quantitative sensitivity. Some of the processes can be simplified by performing them for individual components on an optical bench in air pressure. However, all the really important instrument parameters have to be tested under vacuum with ultraviolet light of the correct wavelength. Additionally, some of the instrument properties may be temperature-dependent. A full thermal test program has to be developed covering the full range of expected instrument temperatures that can be very costly and time-consuming. In most cases such a full program will take around 2 months with the appropriate staffing levels and vacuum chamber availability.

Some of the tests can be repeated in space like the spot size determination or absolute calibration when observing well-characterized UV stars [*Frey et al.*, 2003]. Similar on-orbit calibration can also be performed with solar-pointing instruments [*Hock et al.*, 2012]. A weekly star pointing of the IMAGE FUV instrument was conducted during the whole mission to use stars as an emission standard for the sensitivity trending through all seasons and the full experienced temperature range. With ICON FUV a similar monthly star pointing is planned for the on-orbit verification and sensitivity trending over time.

Acknowledgments
The writing of this publication was supported by NASA's Explorers Program through contracts NNG12FA45C and NNG12FA42I for the ICON project. We want to thank both reviewers for the very careful reading of the manuscript and the many constructive comments about changes that made the final paper clearer. Any data used in this publication can be requested from the corresponding author.

References

Avila, R., et al. (2016), *ACS Instrument Handbook*, pp. 20–32, Version 15.0, STScI, Baltimore, Md.

Corso, A. J., V. Polito, P. Zuppella, S. Zuccon, M. Nardello, P. Nicolosi, J. L. Maria, J. F. Mariscal, E. Quemerais, and M. G. Pelizzo (2013), Extreme and near ultraviolet experimental facility for calibration of space instrumentation, *Proc. SPIE*, *8861*, doi:10.1117/12.2027172.

Davis, M. W., T. K. Greathouse, G. R. Gladstone, K. D. Retherford, D. C. Slater, S. A. Stern, and M. H. Versteeg (2014), Improved ground calibration results from Southwest Research Institute Ultraviolet Radiometric Calibration facility (UV-RCF), *Proc. SPIE*, *9144*, doi:10.1117/12.2057043.

Frey, H. U., S. B. Mende, T. J. Immel, J.-C. Gerard, B. Hubert, S. Habraken, J. Spann, G. R. Gladstone, D. V. Bisikalo, and V. I. Shematovich (2003), Summary of quantitative interpretation of IMAGE far ultraviolet auroral data, *Space Science Reviews*, *109*, 255–283.

Habraken, S., C. Jamar, P. Rochus, S. Mende, and M. Lampton (1997), Optical design of the FUV Spectrographic Imager for the IMAGE mission, *Proc. SPIE*, *3114*, 544–553.

Habraken, S., Y. Houbrechts, E. Renotte, C. A. Jamar, S. B. Mende, H. U. Frey, and O. H. Siegmund (1998), Alignment and performances of the FUV spectrographic imager for the IMAGE mission, *Proc. SPIE*, *3445*, 416–426.

Habraken, S., Y. Houbrechts, E. Renotte, M.-L. Hellin, A. Orban, P. P. Rochus, S. B. Mende, H. U. Frey, S. Geller, and J. M. Stock (1999), Optical calibration of the FUV spectrographic imager for the IMAGE mission, *Proc. SPIE*, *3765*, 508–517.

Hetherington, S., D. Osgood, J. McMann, V. Roberts, J. Gill, and K. McLean (2013), Optical alignment of the Global Precipitation Measurements (GPM) star trackers, *Proc. SPIE*, *8844*, doi:10.1117/12.2024558.

Hock, R. A., P. C. Chamberlin, T. N. Woods, D. Crotser, F. G. Eparvier, D. L. Woodraska, and E. C. Woods (2012), Extreme ultraviolet Variability Experiment (EVE) Multiple EUV Grating Spectrographs (MEGS): Radiometric calibrations and results, *Solar Phys.*, *275*, 145–178, doi:10.1007/s11207-010-9520-9.

Howell, S. B. (2006), *Handbook of CCD Astronomy*, pp. 15–82, Cambridge Univ. Press, Cambrige, U. K.

Kameda, S., et al. (2016), Preflight calibration test results for optical navigation camera telescope (ONC-T) onboard the Hayabusa-2 spacecraft, *Space Science Reviews*, doi:10.1007/s11214-015-0227-y.

Kalmanson, P. C., C. Sarner, and S. Tonnard (2002), Facilities for the calibration, construction, and environmental testing of instruments and detectors in the EUV and FUV, *Proc. SPIE*, *4485*, 303–315.

Larruquert, J. I., J. A. Mendez, J. A. Aznarez, A. S. Tremsin, and O. H. W. Siegmund (2002), Optical properties and quantum efficiency of thin-film alkali halides in the far ultraviolet, *Appl. Opt.*, *41*, 2532–2540.

Loicq, J., C. Kintziger, A. Mazzoli, T. Miller, C. Chou, H. U. Frey, T. J. Immel, and S. B. Mende (2016), Optical design and optical properties of a VUV spectrographic imager for ICON mission, *Proc. SPIE*, *9905*, doi:10.1117/12.2232588.

Mende, S. B. (2016a), Observing the magnetosphere through global auroral imaging. Part 1: Observables, *J. Geophys. Res. Space Physics*, *121*, 10,623–10,637, doi:10.1002/2016JA022558.

Mende, S. B. (2016b), Observing the magnetosphere through global auroral imaging. Part 2: Observing techniques, *J. Geophys. Res. Space Physics*, *121*, 10,638–10,660, doi:10.1002/2016JA022607.

Mende, S. B., et al. (2000a), Far ultraviolet imaging from the IMAGE spacecraft: 2. Wideband FUV imaging, *Space Sci. Rev.*, *91*, 271–285.

Mende, S. B., et al. (2000b), Far ultraviolet imaging from the IMAGE spacecraft: 3. Spectral imaging of Lyman alpha and OI 135.6 nm, *Space Sci. Rev.*, *91*, 287–318.

Mende, S.B., et al. (2017), The far ultra-violet imager on the ICON mission, *Space Science Reviews*, in press.

Morrison, D., L. Paxton, D. Humm, B. Wolven, H. Kil, Y. Zhang, B. Ogorzalek, and C. Mend (2002), On-orbit calibration of the Special Sensor Ultraviolet Scanning Imager (SSUSI)—A far-UV imaging spectrograph on DMSP F16, *Proc. SPIE*, *4485*, 328, doi:10.1117/12.454267.

Peterson, G. L. (2004), Analytic expressions for in-field scattered light distributions, *Proc. SPIE*, *5178*, 184–193, doi:10.1117/12.509120.

Rothman, L. S., et al. (2009), The HITRAN 2008 molecular spectroscopic database, *J. Quant. Spectrosc. Radiat. Transfer*, *110*, 533, doi:10.1016/j.jqsrt.2009.02.013.

Schühle, U. (2003), Cleanliness and calibration stability of UV instruments on SOHO, in *Innovative Telescopes and Instrumentation for Solar Astrophysics*, *Proc. SPIE*, vol. 4853, edited by S. L. Keil and S. V. Avakyan, pp. 88–97.

Vallerga, J. V., and O. H. W. Siegmund (2000), 2K × 2K resolution element photon counting MCP sensor with >200 kHz event rate capability, *Nucl. Inst. Meth. Phys. Res., A*, *442*, 159–163, doi:10.1016/S0168-9002(99)01215-2.

Werner, K. (2010), UV and EUV instruments, in *Landolt-Börnstein, Group VI, Astronomy and Astrophysics*, vol. 4A, pp. 109–119, Springer, Berlin.

Widenhorn, R., M. M. Blouke, A. Weber, A. Rest, and E. Bodegom (2002), Temperature dependence of dark current in a CCD, *Proc. SPIE*, *4669*, 193–201.

Wieman, S., L. Didkovsky, T. Woods, A. Jones, and C. Moore (2016), Sounding rocket observations of active region soft X-ray spectra between 0.5 and 2.5 nm using a modified SDO/EVE instrument, *Sol. Phys.*, *291*, 3567, doi:10.1007/s11207-016-0999-6.

Yan, W., T. Yi, L. Jianpeng, Z. Zhige, and N. Guoqiang (2010), The ground calibration of far ultraviolet scanning imaging spectrometer (FUSIS), *Proc. SPIE*, *7849*, doi:10.1117/12.870475.